Nematic Quantum Criticality in Dirac Systems

Jonas Schwab,[1] Lukas Janssen,[2] Kai Sun,[3] Zi Yang Meng,[4,5] Igor F. Herbut,[6] Matthias Vojta,[2] and Fakher F. Assaad[1]

[1]*Institut für Theoretische Physik und Astrophysik and Würzburg-Dresden Cluster of Excellence ct.qmat, Universität Würzburg, 97074 Würzburg, Germany*

[2]*Institut für Theoretische Physik and Würzburg-Dresden Cluster of Excellence ct.qmat, Technische Universität Dresden, 01062 Dresden, Germany*

[3]*Physics Department, University of Michigan, Ann Arbor, Michigan 48109, USA*

[4]*Department of Physics and HKU-UCAS Joint Institute of Theoretical and Computational Physics, The University of Hong Kong, Pokfulam Road, Hong Kong SAR, China*

[5]*Beijing National Laboratory for Condensed Matter Physics, Institute of Physics, Chinese Academy of Sciences, Beijing 100190, China*

[6]*Department of Physics, Simon Fraser University, Burnaby, British Columbia V5A 1S6, Canada*

(Received 20 October 2021; revised 20 January 2022; accepted 9 March 2022; published 12 April 2022; corrected 7 June 2022)

We investigate nematic quantum phase transitions in two different Dirac fermion models. The models feature twofold and fourfold, respectively, lattice rotational symmetries that are spontaneously broken in the ordered phase. Using negative-sign-free quantum Monte Carlo simulations and an ϵ-expansion renormalization group analysis, we show that both models exhibit continuous phase transitions. In contrast to generic Gross-Neveu dynamical mass generation, the quantum critical regime is characterized by large velocity anisotropies, with fixed-point values being approached very slowly. Both experimental and numerical investigations will not be representative of the infrared fixed point, but of a quasiuniversal regime where the drift of the exponents tracks the velocity anisotropy.

DOI: 10.1103/PhysRevLett.128.157203

In a strongly correlated electron system, global symmetries, such as spin rotation, point group, or translational symmetries, can be spontaneously broken as a function of some external tuning parameter. This challenging problem has been studied extensively numerically and experimentally over the last years and impacts our understanding of quantum criticality [1] in cuprates [2] and heavy fermions [3]. The problem greatly simplifies when the Fermi surface reduces to isolated Fermi points in $2+1$ dimensions and the critical point features emergent Lorentz symmetry. In this context, spin, time reversal, and translational symmetry breaking generically correspond to the dynamical generation of mass terms [4], and the semimetal-to-insulator transition belongs to one of the various Gross-Neveu universality classes [5–11].

Across nematic transitions, rotational symmetry is spontaneously broken [12,13]. For continuum Dirac fermions with Hamiltonian $H(\boldsymbol{k}) = v(k_x\sigma_x + k_y\sigma_y)$ in momentum space, where $\boldsymbol{\sigma}$ are Pauli spin matrices and v is the Fermi velocity, nematic transitions correspond to the dynamical generation of nonmass terms, such as $m\sigma_x$. They shift the position of the Dirac cone and as such break rotational, and therewith also Lorentz, symmetries. Such nematic transitions have been studied theoretically in the past in the context of d-wave superconductors [14–18] and bilayer graphene [19]. Fundamental questions pertaining to the very nature of the transition remain open: While initial renormalization group (RG) calculations based on the ϵ expansion suggested a first-order transition [14,15], a continuous transition has been found in large-N analyses [16,17]. In this Letter, we use quantum Monte Carlo (QMC) simulations and a revised ϵ-expansion analysis to study these transitions. We introduce two different models of Dirac fermions with twofold and fourfold, respectively, lattice rotational symmetries, and demonstrate numerically and analytically that both models feature a continuous nematic transition, realizing a new family of quantum universality classes in Dirac systems *without* emergent Lorentz invariance.

Models.—Inspired from Refs. [13,20,21], we design two models of $(2+1)$-dimensional Dirac fermions, $\mathcal{H}_0$, coupled to a transverse-field Ising model (TFIM),

$$\mathcal{H}_{\mathrm{Ising}} = -J\sum_{\langle \boldsymbol{R},\boldsymbol{R}'\rangle} \hat{s}^z_{\boldsymbol{R}}\hat{s}^z_{\boldsymbol{R}'} - h\sum_{\boldsymbol{R}} \hat{s}^x_{\boldsymbol{R}}, \tag{1}$$

where $\boldsymbol{R}$ denotes a unit cell and $\langle \boldsymbol{R},\boldsymbol{R}'\rangle$ runs over adjacent unit cells. A Yukawa coupling, $\mathcal{H}_{\mathrm{Yuk}}$, between the Ising field and nematic fermion bilinear yields the desired models, $\mathcal{H} = \mathcal{H}_0 + \mathcal{H}_{\mathrm{Ising}} + \mathcal{H}_{\mathrm{Yuk}}$, that correspond to one of many possible lattice regularizations of continuum field theories of Eqs. (4) and (5).

In the C_{2v} model, depicted in Fig. 1(a), we employ a π-flux Hamiltonian on the square lattice as

$$\mathcal{H}_0^{C_{2v}} = -t\sum_{\boldsymbol{R}}\sum_{\sigma=1}^{N_\sigma} \hat{a}^\dagger_{\boldsymbol{R},\sigma}\Big(\hat{b}_{\boldsymbol{R},\sigma}e^{-i\frac{\pi}{4}} + \hat{b}_{\boldsymbol{R}+\boldsymbol{e}_-,\sigma}e^{i\frac{\pi}{4}} + \hat{b}_{\boldsymbol{R}+\boldsymbol{e}_--\boldsymbol{e}_+,\sigma}e^{-i\frac{\pi}{4}} + \hat{b}_{\boldsymbol{R}-\boldsymbol{e}_+,\sigma}e^{i\frac{\pi}{4}}\Big) + \mathrm{H.c.}, \tag{2a}$$

where $\hat{a}$ and $\hat{b}$ with spin index σ are fermion annihilation operators on the two sublattices, t is the hopping parameter, and $N_\sigma = 2$ is the number of spin degrees of freedom. $\mathcal{H}_0$ features two inequivalent Dirac points per spin component in the Brillouin zone (BZ). The Ising spins $\hat{s}_{\boldsymbol{R}}$ couple, with the sign structure indicated in Fig. 1(a), to the nearest-neighbor fermion hopping terms,

$$\mathcal{H}^{C_{2v}}_{\mathrm{Yuk}} = -\xi \sum_{\boldsymbol{R}} \sum_{\sigma=1}^{N_\sigma} \hat{s}^z_{\boldsymbol{R}} \hat{a}^\dagger_{\boldsymbol{R},\sigma} \Big(\hat{b}_{\boldsymbol{R},\sigma} e^{-i\frac{\pi}{4}} - \hat{b}_{\boldsymbol{R}+\boldsymbol{e}_-,\sigma} e^{i\frac{\pi}{4}} - \hat{b}_{\boldsymbol{R}+\boldsymbol{e}_- -\boldsymbol{e}_+,\sigma} e^{-i\frac{\pi}{4}} + \hat{b}_{\boldsymbol{R}-\boldsymbol{e}_+,\sigma} e^{i\frac{\pi}{4}} \Big) + \mathrm{H.c.}, \tag{2b}$$

where ξ denotes the coupling strength. The model has a C_{2v} point group symmetry, composed of reflections, $\hat{T}_\pm$ on the $\boldsymbol{e}_\pm = \boldsymbol{e}_x \pm \boldsymbol{e}_y$ axis. $\hat{T}_\pm$ pins the Dirac cones to the $\boldsymbol{K}_\pm = (\pi/2, \pm\pi/2)$ points in the BZ. Aside from the above reflections, π rotations about the z axis are obtained as $\hat{T}_+\hat{T}_-$. Further, the model exhibits an explicit SU(N_σ) spin symmetry that is enlarged to $O(2N_\sigma)$ [22].

The C_{4v} model corresponds to a bilayer π-flux model, in which the Ising spins are located on the rungs, Fig. 1(b). The fermion hopping Hamiltonian is

$$\mathcal{H}^{C_{4v}}_0 = -t \sum_{\boldsymbol{R}} \sum_{\sigma=1}^{N_\sigma} \hat{a}^\dagger_{\boldsymbol{R},\sigma} (\hat{b}_{\boldsymbol{R}+\boldsymbol{e}_x,\sigma} e^{i\frac{\pi}{4}} + \hat{b}_{\boldsymbol{R}-\boldsymbol{e}_x,\sigma} e^{i\frac{\pi}{4}} + \hat{b}_{\boldsymbol{R}+\boldsymbol{e}_y,\sigma} e^{-i\frac{\pi}{4}} + \hat{b}_{\boldsymbol{R}-\boldsymbol{e}_y,\sigma} e^{-i\frac{\pi}{4}}) + \mathrm{H.c.}, \tag{3a}$$

featuring four Dirac cones per spin component. The Yukawa coupling reads

$$\mathcal{H}^{C_{4v}}_{\mathrm{Yuk}} = -\xi \sum_{\boldsymbol{R}} \sum_{\sigma=1}^{N_\sigma} i \hat{s}^z_{\boldsymbol{R}} \hat{a}^\dagger_{\boldsymbol{R},\sigma} \hat{b}_{\boldsymbol{R},\sigma} + \mathrm{H.c.}, \tag{3b}$$

amounting to a coupling of the Ising spins to the interlayer fermion current. The C_{4v} Hamiltonian commutes with $\hat{T}_{\pi/2}$, corresponding to $\pi/2$ rotation about the z axis. The model is invariant under reflections $\hat{T}_x$ and $\hat{T}_y$ along the x and y axes, respectively. Reflections along $\boldsymbol{e}_\pm = \boldsymbol{e}_x \pm \boldsymbol{e}_y$, denoted by $\hat{T}_\pm$, can be derived from $\hat{T}_{\pi/2}$, $\hat{T}_x$, and $\hat{T}_y$, and therefore also leave the model invariant. The model hence has a C_{4v} symmetry. Particle-hole symmetry, imposes $A(\boldsymbol{k}, \omega) = A(-\boldsymbol{k} + \boldsymbol{Q}, -\omega)$, where $\boldsymbol{Q} = (\pi, \pi)$ such that alongside with the C_{4v} symmetry the Dirac cones are pinned to the $\pm\boldsymbol{K}_\pm$ points in the BZ [22].

Lattice mean-field theory.—The key point of both models is that the point group and particle-hole symmetries are tied to the flipping of the Ising spin degree of freedom. In the large-h limit, the ground state has the full symmetry of the model Hamiltonian and at the mean-field level we can set $\langle \hat{s}^z_{\boldsymbol{R}} \rangle = 0$. In this limit, the Dirac cones are pinned by symmetry. In the opposite small-h limit, the Ising spins order, $\langle \hat{s}^z_{\boldsymbol{R}} \rangle \neq 0$. Thereby, the C_{2v} (C_{4v}) symmetry is reduced to $\hat{T}_+$ (C_{2v}). At the mean-field level, this induces a meandering of the Dirac points in the BZ, see Fig. 2(a), and an anisotropy in the Fermi velocities. A detailed account of the mean-field calculations is presented in the Supplemental Material [22], and at this level of approximation the transition turns out to be continuous, in agreement with the large-N analysis [17].

Continuum field theory.—In order to investigate whether the above remains true upon the inclusion of order-parameter fluctuations, we derive corresponding continuum field theories, which are amenable to RG analyses. To leading order in the gradient expansion around the nodal points, we obtain the Euclidean action $S = \int d^2x d\tau (\mathcal{L}_\Psi + \mathcal{L}_\phi)$ with

$$\mathcal{L}^{C_{2v}}_\Psi = \Psi^\dagger_\sigma (\partial_\tau + \gamma_0\gamma_1 v_\parallel \partial_+ + \gamma_0\gamma_2 v_\perp \partial_- + g\phi\gamma_2)\Psi_\sigma \tag{4}$$

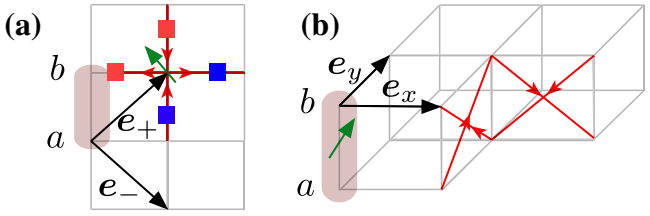

FIG. 1. Sketch of (a) C_{2v} and (b) C_{4v} models, defined on π-flux single-layer and bilayer square lattices, with lattice vectors $\boldsymbol{e}_{+/-}$ and $\boldsymbol{e}_{x/y}$, respectively. Dark pink regions indicate unit cells, containing two orbitals (a and b) and one Ising spin (green arrow) in both cases. Fermions hop along the red lines and acquire a phase factor $e^{i\pi/4}$ when following the direction of the arrow. Red and blue squares in (a) indicate the sign structure in the Yukawa coupling of the C_{2v} model.

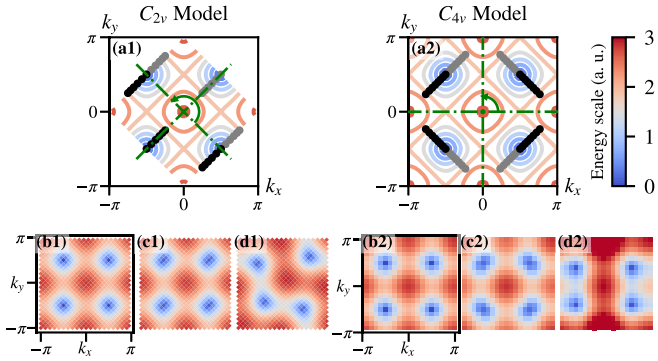

FIG. 2. (a) Contour plot of the fermion dispersion in the disordered phase from mean-field theory. The green lines and arrows indicate the point group symmetries. Black (gray) dots sketch the meandering of the Dirac cones in the nematic phase for $\langle \hat{s}^z_{\boldsymbol{R}} \rangle > 0$ (< 0). (b)–(d) Fermion dispersion from QMC at $L = 20$ for (b) $h = 5.0 > h_c$ featuring isotropic Fermi velocities (c) $h \simeq h_c$, $h \approx 3.27$ (left) and $h \approx 3.65$ (right), and (d) at $h = 1.0 < h_c$ featuring broken point-group symmetries. Color scale applies to all plots.

for the four-component Dirac spinors $\Psi_\sigma \equiv (\hat{a}_\sigma^+, \hat{b}_\sigma^+, \hat{a}_\sigma^-, \hat{b}_\sigma^-)^\top$ in the C_{2v} model, where $\hat{a}_\sigma^\pm$ and $\hat{b}_\sigma^\pm$ corresponds to hole excitations near $\mathbf{K}_\pm$ on the A and B sublattices, respectively, and

$$\mathcal{L}_\Psi^{C_{4v}} = \Psi_\sigma^\dagger [\partial_\tau + \tilde{\gamma}_0(\tilde{\gamma}_1 v_\parallel \oplus \tilde{\gamma}_2 v_\perp)\partial_+ + \tilde{\gamma}_0(\tilde{\gamma}_2 v_\perp \oplus \tilde{\gamma}_1 v_\parallel)\partial_- + g\phi(\tilde{\gamma}_2 \oplus \tilde{\gamma}_2)]\Psi_\sigma \quad (5)$$

for the eight-component Dirac spinors $\Psi_\sigma \equiv (\hat{a}_\sigma^{++}, \hat{b}_\sigma^{++}, \hat{a}_\sigma^{-+}, \hat{b}_\sigma^{-+}, \hat{a}_\sigma^{+-}, \hat{b}_\sigma^{+-}, \hat{a}_\sigma^{--}, \hat{b}_\sigma^{--})^\top$ in the C_{4v} model, where $\hat{a}_\sigma^{+\pm}$ and $\hat{b}_\sigma^{+\pm}$ ($\hat{a}_\sigma^{-\pm}$ and $\hat{b}_\sigma^{-\pm}$) correspond to hole excitations near $\boldsymbol{K}_\pm$ ($-\boldsymbol{K}_\pm$). In the above Lagrangians, we have assumed the summation convention over repeated indices, and $\oplus$ denotes the matrix direct sum. The Fermi velocities $v_\parallel$ and $v_\perp$ correspond to the directions parallel and perpendicular to the shift of the Dirac cones in the ordered phase, with $v_\parallel = v_\perp \sim t$ at the UV cutoff scale Λ. $\partial_\pm$ denotes the spatial derivative in the direction along $\boldsymbol{K}_\pm$. The two sets of Dirac matrices γ_μ, $\tilde{\gamma}_\mu$ realize four-dimensional representations of the Clifford algebra $\{\gamma_\mu, \gamma_\nu\} = \{\tilde{\gamma}_\mu, \tilde{\gamma}_\nu\} = 2\delta_{\mu\nu}$, $\mu, \nu = 0, 1$, and 2. The fermions couple via $g \sim \xi$ to the Ising order-parameter field ϕ, the dynamics of which is governed by the usual ϕ^4 Lagrangian, $\mathcal{L}_\phi = \frac{1}{2}\phi(r - \partial_\tau^2 - c_+^2\partial_+^2 - c_-^2\partial_-^2)\phi + \lambda\phi^4$, with the tuning parameter r, the boson velocities $c_\pm$, and the bosonic self-interaction λ.

ϵ expansion.—The presence of a unique upper critical spatial dimension of three allows an $\epsilon = 3 - d$ expansion, with $\epsilon = 1$ corresponding to the physical case. Because of the lack of Lorentz and continuous spatial rotational symmetries in the low-energy models, it is useful to employ a regularization in the frequency only, which allows us to rescale the different momentum components independently, and evaluate the loop integrals analytically [22]. Two central properties of nematic quantum phase transitions in Dirac systems are revealed by the one-loop RG analysis: First, both models admit a stable fixed point featuring anisotropic power laws of the fermion and order parameter correlation functions. In the C_{2v} model, both components of the Fermi velocity remain finite at the stable fixed point with $0 < v_\parallel^* < v_\perp^*$. At the critical point, a unique timescale τ emerges for both fields Ψ and ϕ [30,31], which scales with the two characteristic length scales ℓ_+ and ℓ_- as $\tau \sim \ell_+^{z_+} \sim \ell_-^{z_-}$, with associated dynamical critical exponents $z_\pm = [1 - \frac{1}{2}\eta_\phi + \frac{1}{2}\eta_\pm]^{-1}$ as $(z_+, z_-) = (1 + 0.3695\epsilon, 1 + 0.1086\epsilon) + \mathcal{O}(\epsilon^2)$, reflecting the absence of Lorentz and rotational symmetries at criticality. By contrast, in the C_{4v} model, the fixed point is characterized by a maximal velocity anisotropy with $(v_\parallel^*, v_\perp^*) = (0, 1)$ in units of fixed boson velocities $c \equiv c_+ = c_- = 1$. This result is consistent with the large-N RG analysis in fixed $d = 2$ [16]. The fact that $v_\parallel^*$ vanishes leads to the interesting behavior that the fixed-point couplings g_*^2 and λ_* are bound to vanish in this case as well. This happens in a way that the ratio $(g^2/v_\parallel)_*$ remains finite, such that the boson anomalous dimensions become $\eta_\phi = \eta_+ = \eta_- = \epsilon$. Importantly, as the fixed-point couplings g_*^2 and λ^* vanish, we expect the one-loop result for the critical exponents to hold at *all* loop orders in the C_{4v} model. For the correlation-length exponent, we find $1/\nu = 2 - \epsilon$. The remaining exponents can then be computed by assuming the usual hyperscaling relations [32]. The susceptibility exponent, for instance, becomes $\gamma = 1$, independent of ϵ. This result is again consistent with the large-N calculation and has previously already been argued to hold exactly [16]. We note that the values of the exponents in the C_{4v} model are independent of the number of spinor components, in contrast to the situation in the C_{2v} model, as well as to the usual Gross-Neveu universality classes [7–10,21,33]. The unique dynamical critical exponent in the C_{4v} model becomes $z = 1$. We emphasize, however, that the critical point still does *not* feature emergent Lorentz symmetry [34] due to the anisotropic fermion spectral function. The second important property revealed by the RG analysis is that the stable fixed points in both models are approached only extremely slowly as function of RG scale, Fig. 3. This is universally true for the C_{4v} model, in which case $v_\parallel$ corresponds to a marginally irrelevant parameter, hence scaling only logarithmically to zero while other irrelevant operators rapidly die out. This defines a quasiuniversal flow [35,36] in which only the velocity anisotropy and not the initial ultraviolet values of other parameters determine the slow drift of the exponents. The RG suggests that this regime emerges at scales $1/b \lesssim 0.05$ (see Ref. [22]), such that it will dominate numerical as well as experimental realizations of this critical phenomena. For a reasonable set of ultraviolet starting values and $\epsilon = 1$, we find that the effective correlation-length exponent $1/\nu_{\text{eff}}$ (anomalous dimension η_ϕ^{eff}) approaches one from above (below), with sizable deviations at intermediate RG scales, see Ref. [22] for details. Moreover, we also

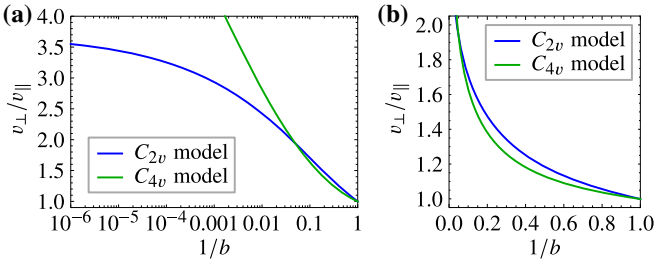

FIG. 3. Ratio of Fermi velocities $v_\perp/v_\parallel$ as function of RG scale $1/b$ for both models. We assume ultraviolet initial values of $v_\parallel(b = 1) = v_\perp(b = 1) = 0.25$, and set $g^2/(v_\parallel v_\perp)(b = 1)$ to the value at the respective stable fixed point. (a) Semilogarithmic, (b) linear plots. Starting at a temperature scale representative of the ultraviolet initial parameters, one has to cool the system by 2 orders of magnitude to *start* observing the differences between both models.

observe that the initial flows at high energy in the two models resemble each other, despite the fact that they substantially deviate from each other at low energy. This suggests that the flow is generically slow in the C_{2v} model as well.

QMC setup.—For the numerical simulations, we used the ALF program package [37] that provides a general implementation of the finite-temperature auxiliary field QMC algorithm [38–40]. To formulate the path integral, we use a Trotter decomposition with time step $\Delta_\tau t = 0.1$ and choose a basis where $\hat{s}^z_{\boldsymbol{R}}|s_{\boldsymbol{R}}\rangle = s_{\boldsymbol{R}}|s_{\boldsymbol{R}}\rangle$. The configuration space is that of a $(2+1)$-dimensional Ising model and we use a single-spin-flip update to sample it. As shown in the Supplemental Material [22] both models are negative-sign-problem free for all values of N_σ [41]. For our simulations, we have used an inverse temperature $\beta = 4L$ for $L \times L$ lattices, and have checked that this choice of β reflects ground-state properties. For the results shown in the main text, we have fixed the parameters as $J = t = 1$ and $N_\sigma = 2$. In the C_{2v} model, we choose $\xi = 0.25$, as larger values of ξ lead to spurious size effects that could falsely be interpreted as first-order transitions, see Ref. [21] and the Supplemental Material [22] for a detailed discussion. In the C_{4v} model, we set $\xi = 1$. As shown in Ref. [22], other values of ξ and N_σ do not alter the continuous nature of the transition.

QMC results.—We compute the spin structure factor, $S(\mathbf{k}) = \sum_{\mathbf{R}} e^{i\mathbf{k}\cdot R}\langle \hat{s}^z_{\mathbf{0}}\hat{s}^z_{\mathbf{R}}\rangle$, the spin susceptibility, $\chi(\mathbf{k}) = \sum_{\mathbf{r}} e^{i\mathbf{k}\cdot\mathbf{R}} \int_0^\beta d\tau \langle \hat{s}^z_{\mathbf{R}}(\tau)\hat{s}^z_{\mathbf{0}}(0)\rangle$ and moments of the total spin $\hat{s}^z = \sum_{\mathbf{R}} \hat{s}^z_{\mathbf{R}}$ to derive RG-invariant quantities such as the correlation ratio [42],

$$R_O = 1 - \frac{O(\boldsymbol{k}_{\min})}{O(\boldsymbol{k} = \mathbf{0})} \quad \text{with} \quad O = S, \chi, \tag{6}$$

and the Binder ratio, $B = \{3 - [\langle(\hat{s}^z)^4\rangle/\langle(\hat{s}^z)^2\rangle^2]\}/2$. Here, $\boldsymbol{k}_{\min}$ corresponds to the longest wavelength on a given finite-size lattice. From the single-particle Green's function, we can extract quantities such as the fermion dispersion relation and Fermi velocities.

At a quantum critical point, RG-invariant quantities follow the form $f[L^z/\beta, (h-h_c)L^{1/\nu}, L^{-\Delta z}, L^{-\omega}]$ [22]. Here we have taken into account the possibility of two characteristic length scales: $\Delta z = 1 - z_-/z_+$. Since our temperature is representative of the ground state, we can neglect the dependence on L^z/β. Up to corrections to scaling, ω, and the possibility of $z_- \neq z_+$, which would result in another correction to scaling term, the data for different lattice sizes cross at the critical field h_c. Figures 4(c) and 4(d) show the crossing points between L and $L + \Delta L$ lattices, with $\Delta L = 2$ (4) for the C_{2v} (C_{4v}) model. As apparent, we obtain consistent results for h_c when considering different RG-invariant quantities. We estimate the correlation-length exponents $1/\nu$ by data collapse for the two models in Figs. 4(a) and 4(b). Considering values of

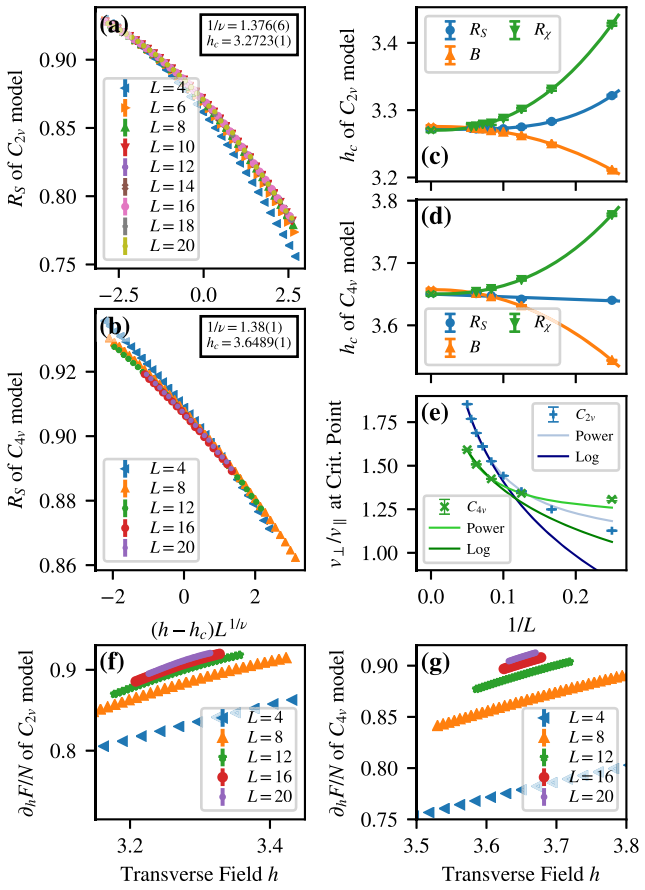

FIG. 4. (a) R_S as function of $(h-h_c)L^{1/\nu}$ for the C_{2v} model, revealing data collapse for $L \gtrsim 12$, assuming $1/\nu = 1.376$. (b) Same as (a), but for C_{4v} model, assuming $1/\nu = 1.38$. (c) Crossing points of different RG-invariant quantities as function of $1/L$ with $\Delta L = 2$ in C_{2v} model, indicating a unique critical point $h_c = 3.27$ for $L \to \infty$. (d) Same as (c), but for C_{4v} model and $\Delta L = 4$, extrapolating to $h_c = 3.65$ (e). Ratio of Fermi velocities $v_\perp/v_\parallel$ as function of $1/L$ at h_c, revealing that the velocity anisotropy increases with increasing system size. The solid lines show power law fits for $L \geq 8$ and logarithmic fits for $L \geq 12$. (f),(g) Derivative of free energy as function of h, exhibiting no discontinuities.

$L \geq L_{\min} = 12$ we obtain $1/\nu = 1.376(6)$ [$1/\nu = 1.38(1)$] for the C_{2v} (C_{4v}) model. These values are in the ballpark of the ϵ-expansion results in the quasiuniversal regime [22]. The data for various values of $L_{\min}$ are given in the Supplemental Material [22], and stand in agreement with the above values. Although seemingly converged, the fact that the velocity anisotropy is expected to flow extremely slowly suggest that the exponents are subject to considerable size effects, see below. Figures 4(f) and 4(g) show the derivative of the free energy with respect to the tuning parameter, $\partial F/\partial h$, confirming the absence of any discontinuity at h_c. The impact of critical fluctuations on the fermion spectrum is displayed in Figs. 2(b) and 2(c). In the disordered phase, Fig. 2(b), the dispersion relation exhibits

rotational symmetry around the Dirac points. On the other hand, at criticality, Fig. 2(c), the dispersion relation suggests a velocity anisotropy, $v_{\parallel} < v_{\perp}$ at the Dirac point. Figure 4(e) demonstrates that this anisotropy grows as a function of system size, in qualitative agreement with the RG predictions. Although our system sizes are too small to detect convergence or divergence of the velocity ratio, we find it reassuring that its dependence on system size qualitatively resembles the scale dependence predicted from the integrated RG flow; cf. Fig. 4(e) with Fig. 3.

Summary.—Both the ϵ-expansion analysis and the QMC simulations show that our two symmetry distinct models of Dirac fermions support continuous nematic transitions. In both cases, the key feature of the quantum critical point is a velocity anisotropy that is best seen in the QMC data of Fig. 2(c). For the C_{4v} model, the ϵ-expansion shows that it diverges logarithmically with system size, in agreement with previous large-N results [16]. This law is supported by finite-size analysis based on QMC data up to linear system size $L = 20$, which is close to the upper bound allowed by current computational approaches. Since the effective exponents flow with the velocity anisotropy, we foresee that lattice sizes beyond the reach of our numerical approach and experiments at ultralow temperatures will be required to obtain converged values. The QMC data captures a quasiuniversal regime [35,36], in which irrelevant operators aside from the velocity anisotropy die out. In fact, the RG prediction for exponents in this intermediate-energy regime is roughly consistent with the finite-size QMC measurements, Fig. 9(c) of Ref. [22]. Furthermore, for a reasonable set of starting values, the integrated RG flows of the two models are initially very similar and deviate from each other only at very low energy scales. A similar behavior of the two models is also observed in the QMC data.

An advantage of our models is that the Dirac points are pinned by symmetry, such that QMC approaches that take momentum-space patches around these points into account [43] represent an attractive direction for future work. Our models equally allow for large-N generalizations, such that QMC and analytical large-N calculations can be compared as a function of increasing N. Finally, we can make contact to nematic transitions in $(2 + 1)$-dimensional Fermi liquids [12,13], since our models do not suffer from the negative-sign problem under doping.

This research has been funded by the Deutsche Forschungsgemeinschaft (DFG) through the Würzburg-Dresden Cluster of Excellence on Complexity and Topology in Quantum Matter *ct.qmat*—Project No. 390858490 (L. J., M. V., F. F. A.), the SFB 1170 on Topological and Correlated Electronics at Surfaces and Interfaces—Project No. 258499086 (J. S., F. F. A.), the SFB 1143 on Correlated Magnetism—Project No. 247310070 (L. J., M. V.), the Emmy Noether program—Project No. 411750675 (L. J.), the National Science and Engineering Council (NSERC) of Canada (I. F. H.), and Grant No. AS 120/14-1 (F. F. A.). Z. Y. M. acknowledges the Research Grants Council of Hong Kong China (Grants No. 17303019, No. 17301420, No. 17301721 and No. AoE/P-701/20) and the Strategic Priority Research Program of the Chinese Academy of Sciences (Grant No. XDB33000000), the K. C. Wong Education Foundation (Grant No. GJTD-2020-01) and the Seed Funding Quantum-Inspired explainable-AI at the HKU-TCL Joint Research Centre for Artificial Intelligence. We are grateful to the Gauss Centre for Supercomputing e.V. for providing computing time on the GCS Supercomputer SUPERMUC-NG at Leibniz Supercomputing Centre.

[1] S. Sachdev, *Quantum Phase Transitions*, 2nd ed. (Cambridge University Press, Cambridge, England, 2011).
[2] S. Sachdev, Colloquium: Order and quantum phase transitions in the cuprate superconductors, Rev. Mod. Phys. **75**, 913 (2003).
[3] H. v. Löhneysen, A. Rosch, M. Vojta, and P. Wölfle, Fermi-liquid instabilities at magnetic quantum phase transitions, Rev. Mod. Phys. **79**, 1015 (2007).
[4] S. Ryu, C. Mudry, C.-Y. Hou, and C. Chamon, Masses in graphenelike two-dimensional electronic systems: Topological defects in order parameters and their fractional exchange statistics, Phys. Rev. B **80**, 205319 (2009).
[5] D. J. Gross and A. Neveu, Dynamical symmetry breaking in asymptotically free field theories, Phys. Rev. D **10**, 3235 (1974).
[6] I. F. Herbut, Interactions and Phase Transitions on Graphene's Honeycomb Lattice, Phys. Rev. Lett. **97**, 146401 (2006).
[7] I. F. Herbut, V. Juričić, and O. Vafek, Relativistic Mott criticality in graphene, Phys. Rev. B **80**, 075432 (2009).
[8] L. Janssen and I. F. Herbut, Antiferromagnetic critical point on graphene's honeycomb lattice: A functional renormalization group approach, Phys. Rev. B **89**, 205403 (2014).
[9] N. Zerf, L. N. Mihaila, P. Marquard, I. F. Herbut, and M. M. Scherer, Four-loop critical exponents for the Gross-Neveu-Yukawa models, Phys. Rev. D **96**, 096010 (2017).
[10] L. Janssen, I. F. Herbut, and M. M. Scherer, Compatible orders and fermion-induced emergent symmetry in Dirac systems, Phys. Rev. B **97**, 041117 (2018).
[11] S. Ray, B. Ihrig, D. Kruti, J. A. Gracey, M. M. Scherer, and L. Janssen, Fractionalized quantum criticality in spin-orbital liquids from field theory beyond the leading order, Phys. Rev. B **103**, 155160 (2021).
[12] V. Oganesyan, S. A. Kivelson, and E. Fradkin, Quantum theory of a nematic Fermi fluid, Phys. Rev. B **64**, 195109 (2001).
[13] Y. Schattner, S. Lederer, S. A. Kivelson, and E. Berg, Ising Nematic Quantum Critical Point in a Metal: A Monte Carlo Study, Phys. Rev. X **6**, 031028 (2016).
[14] M. Vojta, Y. Zhang, and S. Sachdev, Quantum Phase Transitions in d-Wave Superconductors, Phys. Rev. Lett. **85**, 4940 (2000).

[15] M. Vojta, Y. Zhang, and S. Sachdev, Renormalization group analysis of quantum critical points in d-wave superconductors, Int. J. Mod. Phys. B **14**, 3719 (2000).
[16] Y. Huh and S. Sachdev, Renormalization group theory of nematic ordering in d-wave superconductors, Phys. Rev. B **78**, 064512 (2008).
[17] E.-A. Kim, M. J. Lawler, P. Oreto, S. Sachdev, E. Fradkin, and S. A. Kivelson, Theory of the nodal nematic quantum phase transition in superconductors, Phys. Rev. B **77**, 184514 (2008).
[18] J. Wang, Velocity renormalization of nodal quasiparticles in d-wave superconductors, Phys. Rev. B **87**, 054511 (2013).
[19] S. Ray and L. Janssen, Gross-Neveu-Heisenberg criticality from competing nematic and antiferromagnetic orders in bilayer graphene, Phys. Rev. B **104**, 045101 (2021).
[20] X. Y. Xu, K. Sun, Y. Schattner, E. Berg, and Z. Y. Meng, Non-Fermi Liquid at $(2+1)$D Ferromagnetic Quantum Critical Point, Phys. Rev. X **7**, 031058 (2017).
[21] Y.-Y. He, X. Y. Xu, K. Sun, F. F. Assaad, Z. Y. Meng, and Z.-Y. Lu, Dynamical generation of topological masses in Dirac fermions, Phys. Rev. B **97**, 081110(R) (2018).
[22] See Supplemental Material at http://link.aps.org/supplemental/10.1103/PhysRevLett.128.157203, which includes [23–29].
[23] Z.-X. Li, Y.-F. Jiang, and H. Yao, Fermion-sign-free Majarana-quantum-Monte-Carlo studies of quantum critical phenomena of Dirac fermions in two dimensions, New J. Phys. **17**, 085003 (2015).
[24] E. F. Huffman and S. Chandrasekharan, Solution to sign problems in half-filled spin-polarized electronic systems, Phys. Rev. B **89**, 111101(R) (2014).
[25] C. Wu and S.-C. Zhang, Sufficient condition for absence of the sign problem in the fermionic quantum Monte Carlo algorithm, Phys. Rev. B **71**, 155115 (2005).
[26] D. J. Scalapino, S. R. White, and S. Zhang, Insulator, metal, or superconductor: The criteria, Phys. Rev. B **47**, 7995 (1993).
[27] F. F. Assaad, W. Hanke, and D. J. Scalapino, Temperature derivative of the superfluid density and flux quantization as criteria for superconductivity in two-dimensional Hubbard models, Phys. Rev. B **50**, 12835 (1994).
[28] I. F. Herbut and L. Janssen, Topological Mott Insulator in Three-Dimensional Systems with Quadratic Band Touching, Phys. Rev. Lett. **113**, 106401 (2014).
[29] N. Goldenfeld, *Lectures on Phase Transitions and the Renormalization Group*, 1st ed. (CRC Press, Boca Raton, Florida, 1992).
[30] T. Meng, A. Rosch, and M. Garst, Quantum criticality with multiple dynamics, Phys. Rev. B **86**, 125107 (2012).
[31] L. Janssen and I. F. Herbut, Nematic quantum criticality in three-dimensional Fermi system with quadratic band touching, Phys. Rev. B **92**, 045117 (2015).
[32] I. Herbut, *A Modern Approach to Critical Phenomena* (Cambridge University Press, Cambridge, England, 2007).
[33] Y. Liu, W. Wang, K. Sun, and Z. Y. Meng, Designer Monte Carlo simulation for the Gross-Neveu-Yukawa transition, Phys. Rev. B **101**, 064308 (2020).
[34] B. Roy, V. Juričić, and I. F. Herbut, Emergent Lorentz symmetry near fermionic quantum critical points in two and three dimensions, J. High Energy Phys. 04 (2016) 018.
[35] A. Nahum, J. T. Chalker, P. Serna, M. Ortuño, and A. M. Somoza, Deconfined Quantum Criticality, Scaling Violations, and Classical Loop Models, Phys. Rev. X **5**, 041048 (2015).
[36] A. Nahum, Note on Wess-Zumino-Witten models and quasiuniversality in $2+1$ dimensions, Phys. Rev. B **102**, 201116(R) (2020).
[37] ALF Collaboration, F. F. Assaad, M. Bercx, F. Goth, A. Götz, J. S. Hofmann, E. Huffman, Z. Liu, F. Parisen Toldin, J. S. E. Portela, and J. Schwab, The ALF (Algorithms for Lattice Fermions) project release 2.0. Documentation for the auxiliary-field quantum Monte Carlo code, arXiv:2012.11914.
[38] R. Blankenbecler, D. J. Scalapino, and R. L. Sugar, Monte Carlo calculations of coupled boson-fermion systems., Phys. Rev. D **24**, 2278 (1981).
[39] S. R. White, D. J. Scalapino, R. L. Sugar, E. Y. Loh, J. E. Gubernatis, and R. T. Scalettar, Numerical study of the two-dimensional Hubbard model, Phys. Rev. B **40**, 506 (1989).
[40] F. Assaad and H. Evertz, in *Computational Many-Particle Physics*, Lect. Notes Phys. Vol. 739, edited by H. Fehske, R. Schneider, and A. Weiße (Springer, Berlin Heidelberg, 2008), pp. 277–356.
[41] Z.-X. Li, Y.-F. Jiang, and H. Yao, Majorana-Time-Reversal Symmetries: A Fundamental Principle for Sign-Problem-Free Quantum Monte Carlo Simulations, Phys. Rev. Lett. **117**, 267002 (2016).
[42] R. K. Kaul, Spin Nematics, Valence-Bond Solids, and Spin Liquids in SO(N) Quantum Spin Models on the Triangular Lattice, Phys. Rev. Lett. **115**, 157202 (2015).
[43] Z. H. Liu, X. Y. Xu, Y. Qi, K. Sun, and Z. Y. Meng, Elective-momentum ultrasize quantum Monte Carlo method, Phys. Rev. B **99**, 085114 (2019).

Correction: A statement of thanks was erroneously removed during the proof cycle and has been restored.